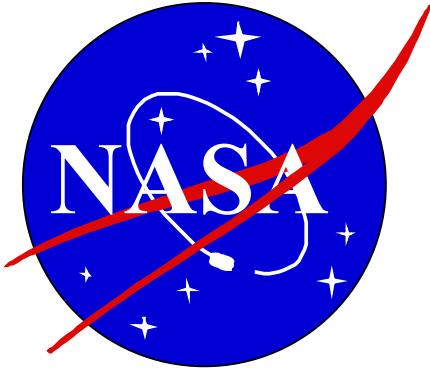


NASA/TM---2002-104606, Vol. 22



**Technical Report Series on Global
Modeling and Data Assimilation**

Max Suarez, Editor

Volume 22

**A Coupled Ocean-Atmosphere Radiative
Model for Global Ocean Biogeochemical
Models**

*Watson W. Gregg
Goddard Space Flight Center, Greenbelt, Maryland*

National Aeronautics and Space Administration

Goddard Space Flight Center
Greenbelt, Maryland 20771

August 2002

Abstract. An ocean-atmosphere radiative model (OARM) evaluates irradiance availability and quality in the water column to support phytoplankton growth and drive ocean thermodynamics. An atmospheric component incorporates spectral and directional effects of clear and cloudy skies as a function of atmospheric optical constituents, and spectral reflectance across the air-sea interface. An oceanic component evaluates the propagation of spectral and directional irradiance through the water column as a function of water, five phytoplankton groups, and chromophoric dissolved organic matter. It tracks the direct and diffuse streams from the atmospheric component, and a third stream, upwelling diffuse irradiance. The atmospheric component of OARM was compared to data sources at the ocean surface with a coefficient of determination (r^2) of 0.97 and a root mean square of 12.1%.

1 Introduction

Knowledge of oceanic irradiance is critical for realistic simulation of ocean biogeochemistry. Since irradiance affects ocean thermodynamics and physiological processes of biota in the oceans, it may affect the abundances and distributions of phytoplankton, and potentially affect the uptake of carbon dioxide.

In order to understand the effects of irradiance on phytoplankton abundances and primary production in the global oceans, we require a reasonably realistic simulation of the irradiance reaching the ocean surface, and propagating through the water column. The simulation must explicitly include the effects of atmospheric optical constituents on surface irradiance, processes occurring at the air-sea interface, and the results of these effects in the water column taking into account the optical properties of the water, phytoplankton, and dissolved detrital materials. In this paper we describe atmospheric and oceanic radiative transfer models, combined as the Ocean-Atmosphere Radiative Model (OARM) that provide a reasonably complex and realistic representation of atmospheric radiative processes and the irradiance availability in the oceans.

2 Ocean-Atmosphere Radiative Model (OARM)

2.1 Atmospheric Component.

The atmospheric radiative model is based on the Gregg and Carder (1990) spectral model for clear skies, and relies on Slingo (1989) for spectral cloud transmittance. The clear sky model of Gregg and Carder (1990) was derived from Bird and Riordan (1986), but was limited to the spectral range of photosynthetically available radiation (PAR), defined as 350-700 nm. It also contained increased spectral resolution and marine atmospheric and surface reflectance conditions. It compared within $\pm 6.6\%$ root mean square (RMS) with surface observations of spectral irradiance and $\pm 5.1\%$ RMS with integrated PAR (Gregg and Carder, 1990). This model is extended for OARM from the PAR spectral domain to the entire solar spectrum, from 200 nm to 4 μm , representing >99% of the total solar irradiance impinging on the top of the atmosphere. For computational efficiency, the spectral resolution is degraded from 1 nm used in Gregg and Carder (1990) to a variable resolution appropriate for the spectral absorbing

properties of the major atmospheric optically active gases, specifically ozone, water vapor, oxygen, and carbon dioxide (Table 1). The spectral resolution is fixed at 25 nm for the PAR range, which is the region of interest for phytoplankton photosynthesis.

A modification to the clear sky model is the use of spectral surface reflectance in the presence of sea foam based on observations by Frouin et al. (1996), and confirmed by Moore et al. (1998). This modification accounts for the fact that some of the reflectance by sea foam is due to bubbles located slightly below the surface. This produces some absorption by sea water before reflecting the light out of the water. Since longer wavelengths are much more strongly absorbing than shorter ones, the net effect is reduction of foam reflectance at longer wavelengths. Based on Frouin's data (Frouin et al., 1996) foam reflectance is treated as

$$F(\lambda) = a_0 + a_1 \ln[T_w(\lambda)] + a_2 \ln[T_w(\lambda)]^2 + a_3 \ln[T_w(\lambda)]^3 ; \lambda < 900 \text{ nm} \quad (1)$$

where F is a factor to adjust foam reflectance for spectral dependence, λ is wavelength in nm, T_w is the transmittance of water

$$T_w = \exp[a_w(\lambda) + 0.5b_w(\lambda)] \quad (2)$$

where a_w and b_w are the spectral absorption and scattering coefficients of seawater, respectively. The 0.5 factor for b_w represents the backscattered portion. In Eq. 1, a_0 , a_1 , a_2 , and a_3 are empirical coefficients to produce a best fit to the published data of Frouin et al. (1996), and are 0.9976, 0.2194, 0.0554, and 0.0067, respectively.

At and above 900 nm, a_w is nearly completely absorbing, and a new parameterization is used

$$F(\lambda) = b_0 + b_1 \lambda + b_2 \lambda^2 + b_3 \lambda^3 ; \lambda \geq 900 \text{ nm} \quad (3)$$

where b_0 , b_1 , b_2 , and b_3 are defined similarly to their counterparts in Eq. 1, and are 5.026, -0.0114 , 9.552×10^{-6} , and -2.698×10^{-9} , respectively.

Total foam reflectance ρ_f now includes spectral dependence through

$$\rho_f(W, \lambda) = \rho_f(W) F(\lambda) \quad (4)$$

where W is the wind speed (m s^{-1}) and $\rho_f(W)$ is defined as in Gregg and Carder (1990). Total surface reflectance is the sum of the specular and foam contributions, which now have a spectral dependence

$$\rho_d(W, \lambda) = \rho_{dsp}(W) + \rho_f(W, \lambda) \quad (5)$$

$$\rho_s(W, \lambda) = \rho_{ssp}(W) + \rho_f(W, \lambda) \quad (6)$$

where ρ_d and ρ_s represent the direct and diffuse surface reflectance components, and the subscript sp represents specular reflectance (Gregg and Carder, 1990).

Under cloudy skies, OARM utilizes the cloudy sky model of Slingo (1989). This model computes irradiance transmittance through clouds based on the liquid water path and the cloud droplet effective radius using a Delta-Eddington approximation of the two-stream approach. It is used for shortwave cloud forcing in the National Center for Atmospheric Research Community Climate Model 3 (Kiehl et al., 1998).

In our implementation of the Slingo (1989) model, gaseous absorption by ozone, oxygen, carbon dioxide, and water vapor, occurs before cloud transmittance, and Earth curvature effects (Kasten, 1966) are accounted for. The cloud droplet radius is set to a

Table 1. Atmospheric optical data for OARM. λ is wavelength (nm), F_o is extraterrestrial irradiance (W/m²), τ_r is Rayleigh optical thickness (dimensionless), a_{oz} is ozone absorption coefficient (cm⁻¹), a_{wv} is water vapor absorption coefficient (cm⁻¹), a_{o_2} is oxygen absorption coefficient (cm⁻¹), and a_{co_2} is carbon dioxide absorption coefficient (cm⁻¹). A data file is available online at [salmo.gsfc.nasa.gov, pub/outgoing/oarm/atmo25.dat](http://salmo.gsfc.nasa.gov/pub/outgoing/oarm/atmo25.dat).

λ	F_o	τ_r	a_{oz}	a_{wv}	a_{o_2}	a_{co_2}
250	16.5280	2.8229	80.8836	0.0000	0.0000	0.0000
325	41.0035	0.8742	0.3584	0.0000	0.0000	0.0000
350	12.7915	0.5925	0.0016	0.0000	0.0000	0.0000
375	27.1180	0.4768	0.0001	0.0000	0.0000	0.0000
400	35.1935	0.3643	0.0000	0.0000	0.0000	0.0000
425	42.1795	0.2833	0.0008	0.0000	0.0000	0.0000
450	49.1940	0.2238	0.0040	0.0000	0.0000	0.0000
475	49.7700	0.1791	0.0121	0.0000	0.0000	0.0000
500	48.3945	0.1451	0.0279	0.0000	0.0000	0.0000
525	46.4935	0.1189	0.0529	0.0000	0.0000	0.0000
550	46.5160	0.0983	0.0832	0.0000	0.0000	0.0000
575	46.1380	0.0820	0.1140	0.0148	0.0000	0.0000
600	44.1230	0.0690	0.1176	0.0851	0.0000	0.0000
625	42.0468	0.0584	0.0967	0.0016	0.0058	0.0000
650	39.5245	0.0498	0.0643	0.0408	0.0000	0.0000
675	37.8730	0.0427	0.0416	0.0009	0.2333	0.0000
700	18.7465	0.0382	0.0261	0.1074	0.1299	0.0000
725	66.8775	0.0319	0.0132	0.1462	0.0000	0.0000
775	59.9900	0.0244	0.0072	0.0065	1.1176	0.0000
850	102.2358	0.0168	0.0020	0.0568	0.0001	0.0000
950	84.7899	0.0108	0.0000	4.9142	0.0000	0.0000
1050	67.8772	0.0072	0.0000	0.0279	0.0002	0.0002
1150	56.0762	0.0050	0.0000	17.5902	0.0000	0.0000
1250	46.1106	0.0032	0.0000	0.0479	0.0028	0.0005
1350	37.3780	0.0026	0.0000	115.3197	0.0000	0.0003
1450	31.8313	0.0020	0.0000	95.2031	0.0000	0.0023
1550	27.2524	0.0015	0.0000	0.0364	0.0000	0.0014
1650	22.7691	0.0012	0.0000	0.0082	0.0000	0.0010
1750	18.6144	0.0009	0.0000	2.0008	0.0000	0.0001
1900	27.9521	0.0007	0.0000	228.9211	0.0000	0.0087
2200	33.6300	0.0004	0.0000	0.2550	0.0000	0.0118
2900	32.5775	0.0001	0.0000	314.7111	0.0000	0.0256
3700	7.2635	0.0000	0.0000	0.9158	0.0000	0.0003

constant 11.8 μm , which represents the mean oceanic value observed in a global survey (Han et al., 1994).

The clear and cloudy sky models track two irradiance streams to the ocean surface: direct and diffuse (Figure 1). The magnitude, spectral, and directional effects of clouds

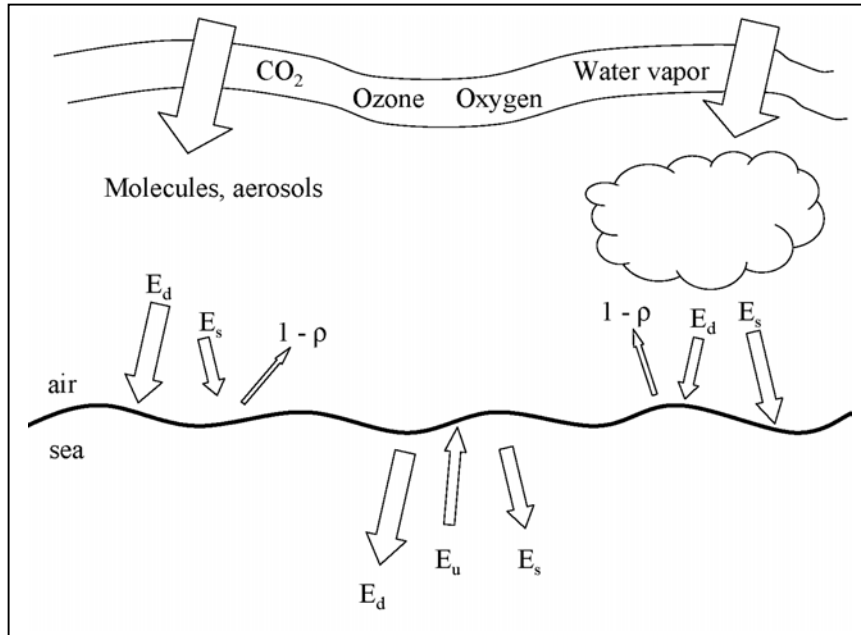


Figure 1. Depiction of the pathways of irradiance under clear and cloudy skies, and in the oceans. The sizes of the arrows indicate the relative proportions of direct (E_d) and diffuse (E_s) irradiance for clear skies and cloudy skies. Some of the surface irradiance is reflected off the sea surface ($1 - \rho$). These pathways continue into the ocean where an additional diffuse upwelling (E_u) path exists.

on irradiance reaching the ocean surface are illustrated in Figure 2 for a liquid water path of 80 g m^{-2} . This water path value produces about one-half the irradiance of clear skies for the same solar zenith angle (30°), atmospheric optical gases and molecular and particulate scattering. Clouds clearly change the amount of irradiance reaching the ocean surface, but also directional quality by apportioning a larger percentage to

diffuse rather than direct, which predominates under clear skies. The spectral effects of clouds are shown more clearly in Table 2, where proportions of different parts of the visible spectrum are listed with and without clouds. Cloudy sky blue spectra (350-400 nm) represent a larger proportion of total PAR than clear sky spectra (20.5%), while cloudy sky red spectra (650-700 nm) represent a smaller proportion (-9.4%). These results confirm observations by Siegel et al. (1999).

OARM requires external cloud properties (cloud cover and liquid water path), as well as surface pressure, wind speeds, relative humidity, precipitable water, and ozone. Climatologies of cloud variables were created using a 5-year record of International Satellite Cloud Climatology Project (ISCCP)-D2 monthly mean data made available by the NASA/Goddard Earth Sciences Distributed Active Archive Center (GES-DAAC). Climatologies of surface pressure, wind speeds, relative humidity, precipitable water were created using National Center for Environmental Prediction (NCEP) Reanalyses for the years 1978-2000 (Kalnay et al., 1996). Climatological ozone was derived from a 20.5 year record beginning in 1978 of several Total Ozone Mapping Spectrometer (TOMS) sensors, again made available by the GES-DAAC.

2.2 Oceanic Component.

The oceanic portion of OARM tracks three irradiance streams in the water column: downwelling direct, downwelling diffuse, and upwelling diffuse (Figure 1). A complete mathematical description of the oceanic component is described in the Appendix. However, the highlights of the model are described in the following.

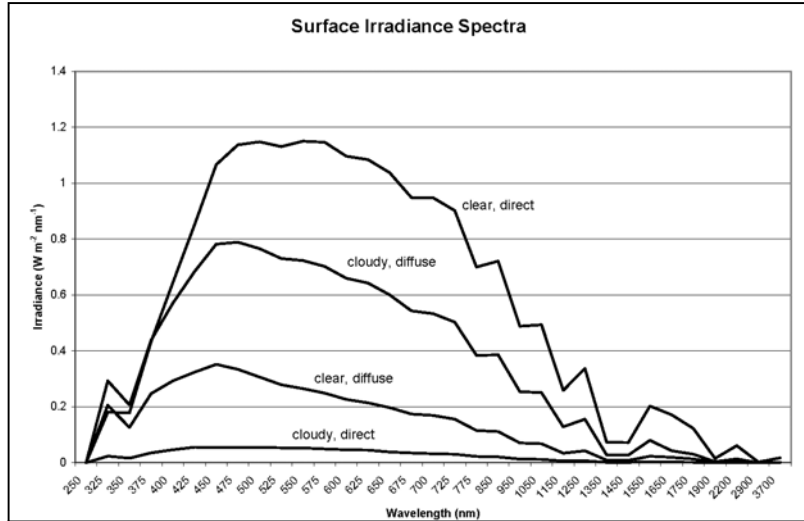


Figure 2. Spectral surface irradiance just below the sea surface (after spectral surface reflectance) for clear skies and cloudy skies. The cloudy sky simulation represents the effects of 80 g m^{-2} liquid water path, which produces about half the total surface solar irradiance as the clear sky model for the same solar zenith angle and atmospheric optical properties.

contributions in the water column and steadily decreases as the result of absorption and scattering processes, the downwelling diffuse irradiance gains forward-scattered downwelling direct irradiance and backscattered upwelling diffuse irradiance in the water column. This irradiance stream travels along a path defined as the average cosine for downwelling diffuse irradiance. This is considered constant in OARM at 0.83 (Sathyendranath and Platt, 1988).

Table 2. Comparison of proportion of blue irradiance to red irradiance under clear and cloudy skies. Cloudy sky used a liquid water path of 80 g m^{-2} , which produces a reduction just under the sea surface of about half that for clear skies.

	Percent of PAR	
	350-400 nm	650-700 nm
Clear	11.2%	17.0%
Cloudy	13.5%	15.4%
Difference	20.5%	-9.4%

direct and downwelling diffuse explicitly included, similarly to Ackleson et al. (1994). The diffuse upwelling stream can represent 10% of the total at some wavelengths. We track only one scattering event for each of the oceanic layers for computational convenience. This approximation is effective for the open ocean domain, but would

The direct downwelling stream contains the irradiance directly transmitted by the sun, traversing the air-sea interface, and proceeding forward at an angle described by the solar zenith angle modified by the refractive index of seawater. Each scattering and absorbing event in the water column removes irradiance from the direct downwelling stream.

Whereas the downwelling direct irradiance receives no contributions in the water column and steadily decreases as the result of absorption and scattering processes, the downwelling diffuse irradiance gains forward-scattered downwelling direct irradiance and backscattered upwelling diffuse irradiance in the water column. This irradiance stream travels along a path defined as the average cosine for downwelling diffuse irradiance. This is considered constant in OARM at 0.83 (Sathyendranath and Platt, 1988).

The diffuse upwelling stream is composed entirely of back-scattered direct and diffuse downwelling irradiance. It is derived from the two-stream model of Aas (1987), with contributions from both the downwelling

become erroneous in waters containing very large amounts of optically active constituents.

Application of the oceanic portion of OARM requires that the absorption and scattering properties of the water column be specified. In this effort we include fixed contributions by seawater and chromophoric dissolved organic matter (CDOM), and variable contributions by five different phytoplankton groups. Water absorption and scattering properties are taken from Smith and Baker (1981) for the range 200-800 nm, Circo and Petty (1951) for the range 800nm-2.5 μ m, and Maul (1985) for the range 2.5–4.0 μ m. A reanalysis of seawater absorption for 380-729 nm (Pope and Fry, 1997), is substituted for the Smith and Baker (1981) estimates (Table 3). CDOM absorption is taken from Carder

et al. (1989), which includes a humic acid component and a fulvic acid component.

Phytoplankton specific absorption coefficients are derived by taking spectra from the published literature and normalizing to the absorption at 440 nm [$a^*_p(440)$] to obtain normalized specific absorption spectra [$a^*_p(\lambda)_N$] for each of the five phytoplankton groups (see Appendix). The resulting spectra exhibit substantial inter-group variability (Figure 3).

Phytoplankton specific scattering coefficients are obtained from measurements at 590 nm and extended to the entire spectrum from information on specific attenuation coefficients (Bricaud et al., 1988; see Appendix). Again substantial group-dependent variability is apparent in the scattering spectra (Figure 3). Additionally, knowledge of the specific

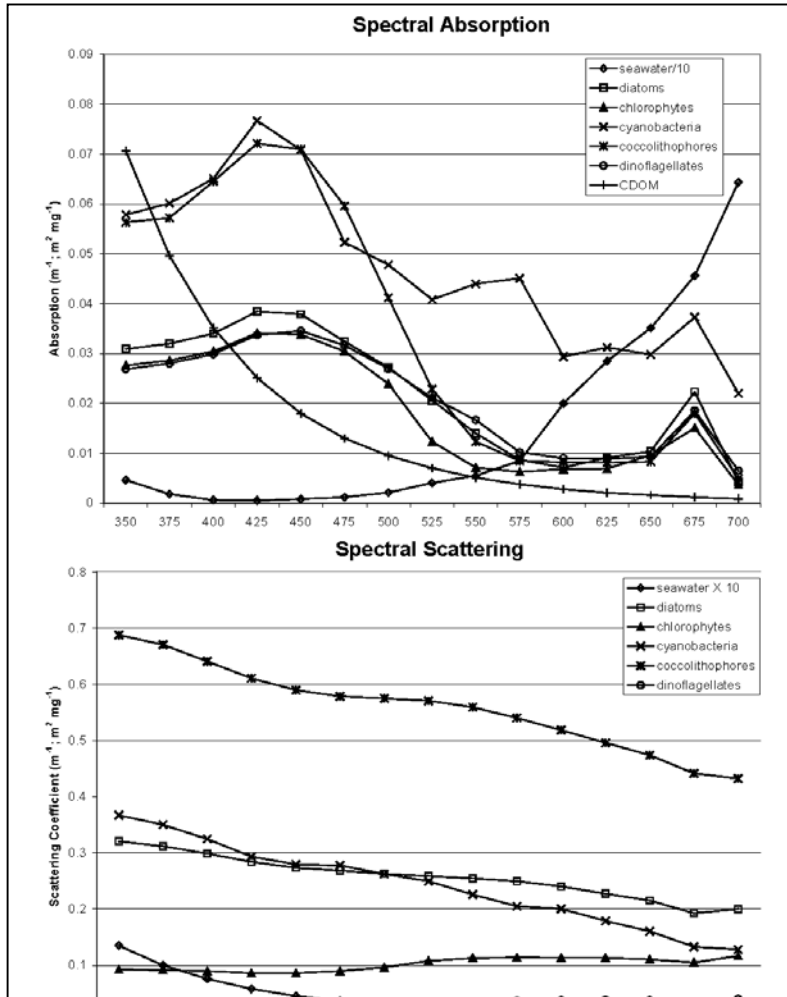


Figure 3. Spectral absorption (top) and scattering (bottom) for oceanic constituents in the oceanic component of OARM. Units for seawater absorption and scattering coefficients are m^{-1} , chlorophyll-specific absorption and scattering coefficients for phytoplankton groups have units of $m^2 mg^{-1}$. Note that seawater absorption coefficients have been scaled by a factor of 0.1, and seawater scattering coefficients have been scaled by a factor of 10 to fit on the plot.

backscattering coefficient is required for the oceanic model. These values are derived from the probability of backscatter (see Appendix).

All calculations are performed in energy units ($W m^{-2}$), in conformance to the absorption and scattering derivations. When summing the mean irradiance in the oceanic

Table 3. Spectral seawater absorption (a_w) and total scattering (b_w) coefficients (m^{-1}). Derived from Smith and Baker (1981) for the spectral ranges 200-370 nm and 730-800 nm, Pope and Fry (1997) for the range 380-720 nm, Circo and Petty (1951) for the range 800nm-2.5 μ m, and Maul (1985) for the range 2.5-4 μ m.

λ (nm)	a_w	b_w
250	0.6112	0.0567
325	0.0762	0.0187
350	0.0461	0.0135
375	0.0182	0.0100
400	0.0063	0.0076
425	0.0051	0.0058
450	0.0083	0.0045
475	0.0119	0.0036
500	0.0215	0.0029
525	0.0407	0.0023
550	0.0550	0.0019
575	0.0849	0.0016
600	0.1995	0.0014
625	0.2850	0.0012
650	0.3512	0.0009
675	0.4559	0.0007
700	0.6433	0.0007
725	1.4449	0.0006
775	2.3900	0.0004
850	3.7382	0.0002
950	27.4805	0.0000
1050	19.3470	0.0000
1150	67.1800	0.0000
1250	94.9976	0.0000
1350	363.1256	0.0000
1450	1118.6070	0.0000
1550	944.8757	0.0000
1650	519.5995	0.0000
1750	646.7179	0.0000
1900	3768.5610	0.0000
2200	2628.0830	0.0000
2900	437623.0000	0.0000
3700	1338404.0000	0.0000

layers of an Ocean General Circulation Model (OGCM), irradiance is converted to quantum flux ($\mu\text{mol quanta m}^{-2} \text{s}^{-1}$) to enable photoadaptation and growth kinetics to occur in accordance with the prevalence of laboratory analyses.

3 Discontinuities in the Cloud Data Set

The ISCCP cloud cover and liquid water path data exhibited spatial discontinuities (Figure 4). These discontinuities typically occurred in three general locations: the central Indian Ocean, western Atlantic Ocean, and the central Pacific Ocean. The Indian Ocean discontinuity was always the most obvious and persistent, the Pacific Ocean discontinuity was second, and the Atlantic Ocean discontinuity was diminished relative to the Indian and often not apparent. The discontinuities were always narrowest at the equator and became wider toward high latitudes (Figure 4). As such, they resembled the coverage typical of geostationary satellites. Similar observations have been noted by Norris (2000). These discontinuities were apparent in nearly every month and year of the data record, although the

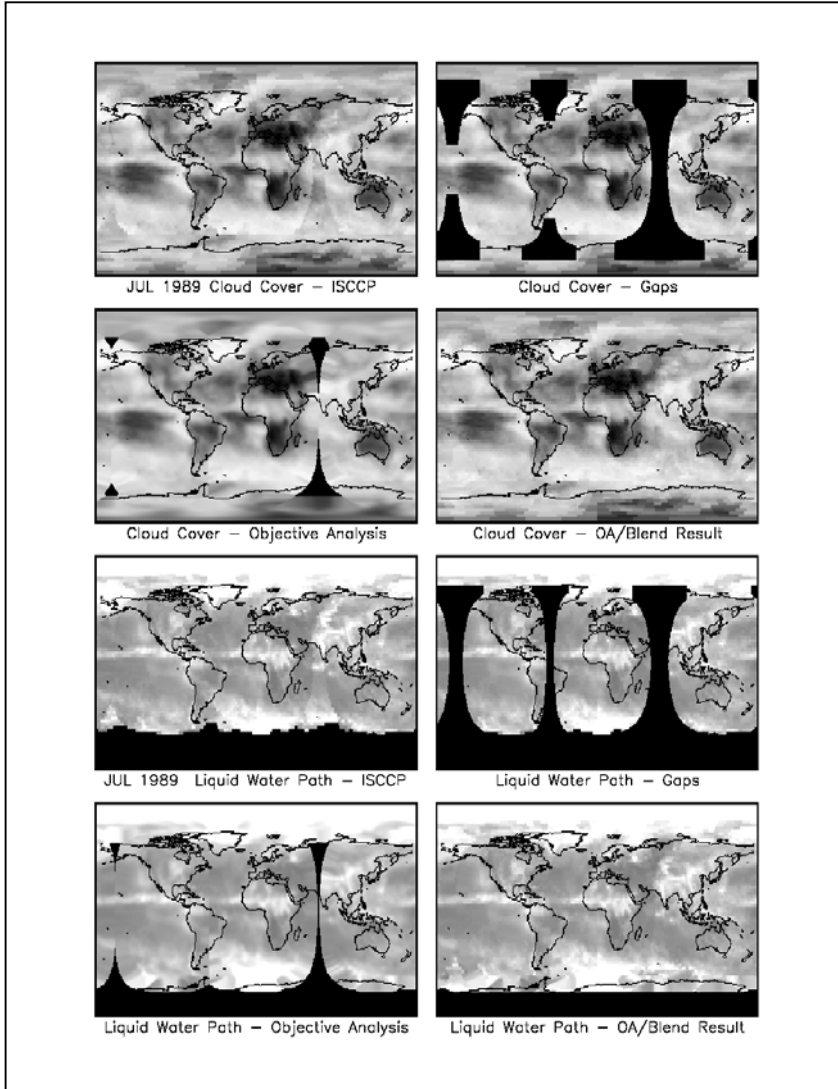


Figure 4. Depiction of the discontinuities in the ISCCP cloud cover (top 4 panels) and liquid water path (bottom 4 panels) data sets for July 1989. This sequence shows the discontinuities in the upper left (note especially the central Indian Ocean), elimination of data occurring in these areas in the upper right, reconstruction using objective analysis in the lower left panel, and the final reconstruction where the edges of the reconstructed gaps are taken from objective analysis to serve as an interior boundary condition for the blended analysis.

locations differed mon-thly on occasion and sometimes differed between the cloud cover and liquid water path data sets.

The ISCCP data set is a compilation of radiances from many different satellites, but is generally derived from two series of geostationary and polar-orbiting missions. The radiances are combined and Level-3 products (geophysical variables such as the cloud cover and liquid water path of interest here) are derived and mapped to a standard Earth grid (Rossow et al., 1996). Although on-orbit failures and launch delays affect the coverage of the Earth by these two satellite series at any one time, there are usually three geostationary satellites, located in the western Pacific near 140°E (the GMS series), in the eastern Atlantic near 0° (the METEOSAT series), and in the eastern Pacific near 90°W (the GOES series). Data from these three geostationary series are the priority for the ISCCP-D2 archive (Rossow et al., 1996). Unfortunately, the GMS and METEOSAT satellites do not cover the central Indian Ocean, which is filled in by the NOAA polar-orbiting series. This geostationary gap lies over the Indian Ocean discontinuity, immediately suggesting a cause. METEOSAT and GOES coverages overlap in the central western Atlantic Ocean, corresponding to the second discontinuity. In cases of overlap, the ISCCP procedures are to preferentially use the data with the lowest solar zenith angle (Rossow et al., 1996). GOES and GMS overlap in the central Pacific again corresponding to the location of the Pacific discontinuity.

Considering the effort devoted to inter-calibration among the diverse satellite sources by the ISCCP project (Rossow et al., 1996), we suspected that these discontinuities resulted from satellite/sensor inter-calibration inconsistencies that may have been too subtle to appear in the Level-1 data but re-appeared in the Level-3 products as a result of extended processing. We attempted to ameliorate the effects of the sensor discontinuities in the Level-3 data, assuming that Level-1 inter-calibration procedures by the ISCCP effort have been exhaustive. We first located the area of discontinuity in each monthly record. We eliminated all values that existed in the apparent discontinuities, by specifying a location in the center of the discontinuity at the equator, and its width, and then re-creating its shape in the mapped Level-3 image by applying a cosine function. The eliminated values produced gaps in the images of cloud cover and liquid water path (Figure 4).

To reconstruct data in the newly created gaps, we first applied the Successive Correction Method (SCM), using the Barnes method (Daley, 1991). We applied a radius of influence of 100 km. This method is often referred to as objective analysis. The SCM re-created data in the gaps in conformance with the spatial structure of the data outside the gaps produced by the geostationary satellites. However, it also produced a new discontinuity at the meridional center of the gaps where the spatial structure trends of the two geostationary satellites were in disagreement (Figure 4). Thus we limited our application of SCM to a small number of gridded pixels inside the gap on each side. The number varied from 4-12 depending upon the size of the gaps, but 4 was used most often. Since these pixels are very close to the valid data provided by the geostationary satellites, we assumed these data to represent a “truth field”, and then applied the blended analysis of Reynolds (1988) to reconstruct the remainder of the gaps. This method produces a bias correction given a set of internal boundary conditions represented by the “truth field”, while adhering to the spatial structure of the original data in the gap area before elimination. This bias correction quality is the desired characteristic sought for this problem. The method has been used successfully in reconstructing sea surface temperature fields from satellite data using *in situ* observations (Reynolds, 1988,

Reynolds et al., 1989), as well as for chlorophyll concentrations (Gregg and Conkright, 2001). The resulting image fields indicated little apparent discontinuity, while retaining spatial structure of the original fields, even in the gap-eliminated regions (Figure 4).

4 Comparison of OARM with Surface Solar Irradiance Data

OARM results were compared to surface solar irradiance data produced by ISCCP (Bishop et al., 1997) to evaluate its performance. The ISCCP surface solar irradiance data represent monthly means integrated over the solar spectrum. OARM is a spectral and directional model over the same spectral domain. The comparison was performed only for the Jan. 1989-May 1991 using coincident monthly mean atmospheric optical variables (not the climatologies discussed earlier). This time period was selected because of the coincident availability of ISCCP cloud data from the GES-DAAC and TOMS ozone data. Although the ISCCP surface solar irradiance data represented the output from a model (Frouin et al., 1989), it has been tested extensively against field measurements with excellent results (Bishop et al., 1997). The comparison performed here involved integrating the surface spectral irradiance computations of OARM across the entire solar spectrum and over the direct and diffuse components, with surface reflectance neglected. Thus we effected a one-to-one comparison with data, that indicated the performance of the spectral and directional OARM.

The comparison between OARM integrated spectral and directional irradiance exhibited a large degree of correspondence with ISCCP surface solar irradiance for the 29 month record under investigation (Table 4). Mean coefficient of determination (r^2) was 0.97, with RMS of 12.1% and an average error of -4.0%. Minimum and maximum r^2 was 0.96 and 0.98, respectively. The minimum RMS was 9.9% occurring in Jun. 1989 and the maximum was 15.1% occurring in Mar. 1990. The maximum was primarily the result of disagreements occurring in the Antarctic Ocean. The minimum average error was -7.3% and the maximum was -1.2%. The negative sign on the average error indicates bias: OARM was typically lower than ISCCP.

Table 4. Comparison of OARM surface solar irradiance integrated over the solar spectrum and over direct and diffuse components with total surface solar irradiance data from ISCCP over a 29-month period from Jan. 1989 to May 1991.

	Mean	Minimum	Maximum
r^2	0.97	0.96	0.98
RMS	12.1%	9.9%	15.1%
Average error	-4.0%	-7.3%	-1.2%

Representative scatterplots of OARM and ISCCP total surface irradiance for four seasons indicated the correspondence between the two (Figure 5). The vast majority of the points in each month fall on a one-to-one line, but OARM had a substantial number of lower computed irradiances in the mid-range (about 120-250 $W m^{-2}$) than ISCCP. Outliers well below the one-to-one line indicated differences in ice masking data sets used here: ISCCP used a radiance threshold (Bishop et al., 1997) while OARM used ice sheet distributions from the NASA Data Assimilation Office. In Feb. 1990, Aug. 1990, and Nov. 1989 the comparison indicated slightly higher estimates by OARM at low

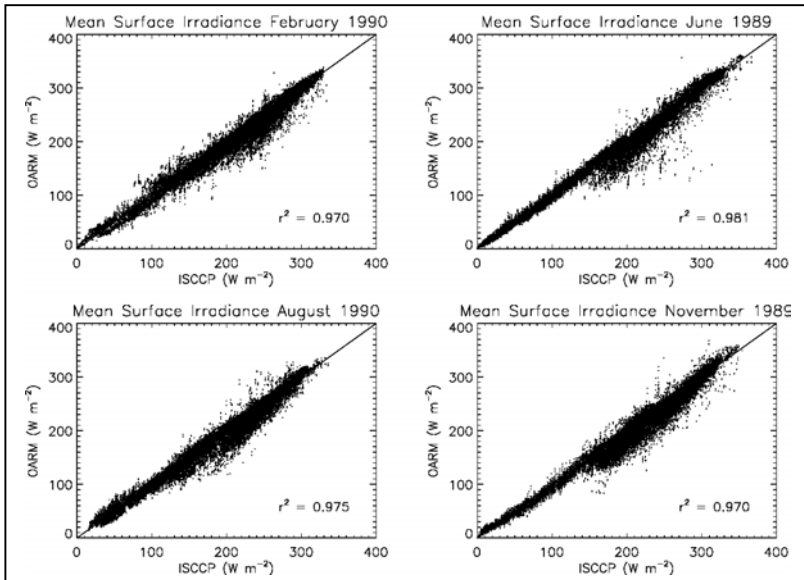


Figure 5. Scatterplots of surface irradiance produced by OARM integrated over the entire solar spectral domain and over the direct and diffuse paths, and the ISCCP data for 4 representative months

irradiance levels ($< 50 \text{ W m}^{-2}$) than ISCCP. This was due to Earth curvature effects that were accounted for in OARM, but not in ISCCP.

Distributions of integrated surface irradiance for Feb. and Sep. 1990 (Figures 6 and 7) illustrated the nature of the agreement between OARM and the ISCCP data sets. General features of surface irradiance were in agreement throughout the global domain, especially over the oceanic portions.

The ISCCP data exhibited smoothing of the retrieved radiance fields (J.K.B. Bishop, personal communication, 1999). The input cloud fields used by OARM were not smoothed. This gave rise to some of the differences observed in the statistical analyses. Overall, these distributions of surface integrated irradiance reflected the correspondence observed in the statistical analyses.

Acknowledgements. We wish to thank NOAA/NCEP for Reanalysis products (surface pressure, wind speed, relative humidity, and precipitable water), NASA/GES-DAAC for providing ISCCP cloud and TOMS ozone products, the ISCCP project for producing the cloud data, and the NASA TOMS Project for producing and distributing the ozone data. Nancy Casey (Science Systems and Applications, Inc., Lanham, MD) provided graphical analysis, plots, and analysis of ISCCP cloud cover and liquid water path data. This work was supported under NASA Grant (RTOP) 971-622-51-31. Atmospheric and oceanic optical data described in this paper are available via anonymous ftp at [salmo.gsfc.nasa.gov](ftp://salmo.gsfc.nasa.gov/pub/outgoing/oarm), in `pub/outgoing/oarm`.

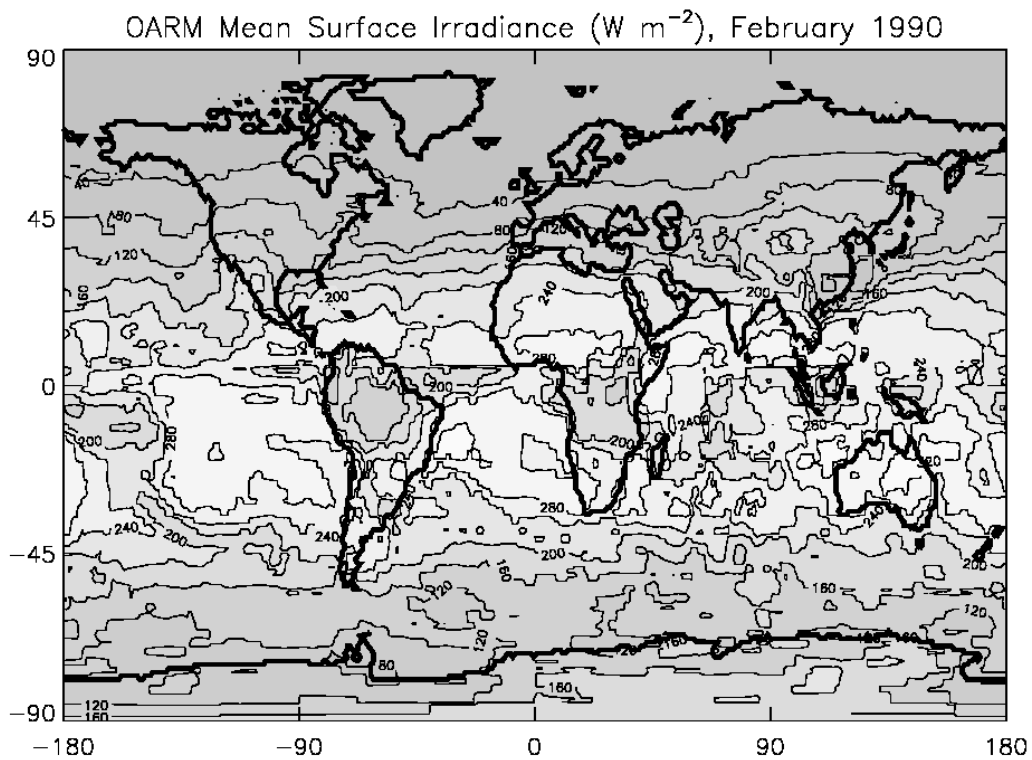
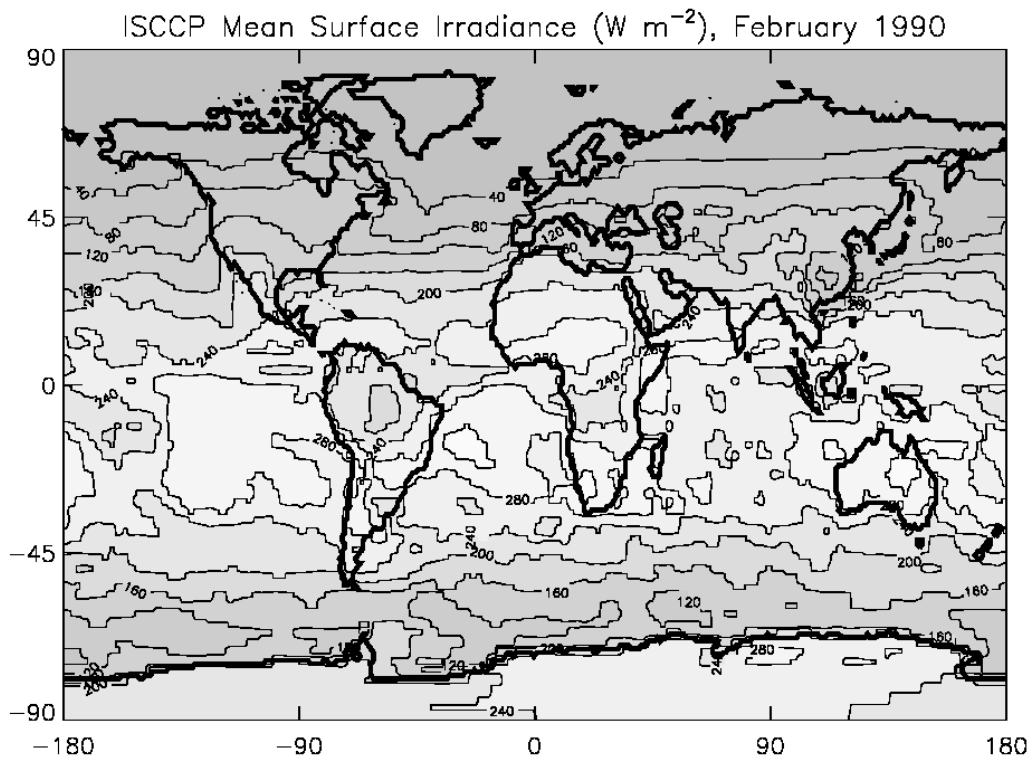


Figure 6. Contour image of total surface irradiance from ISCCP for February 1990 and the spectrally and directionally integrated OARM.

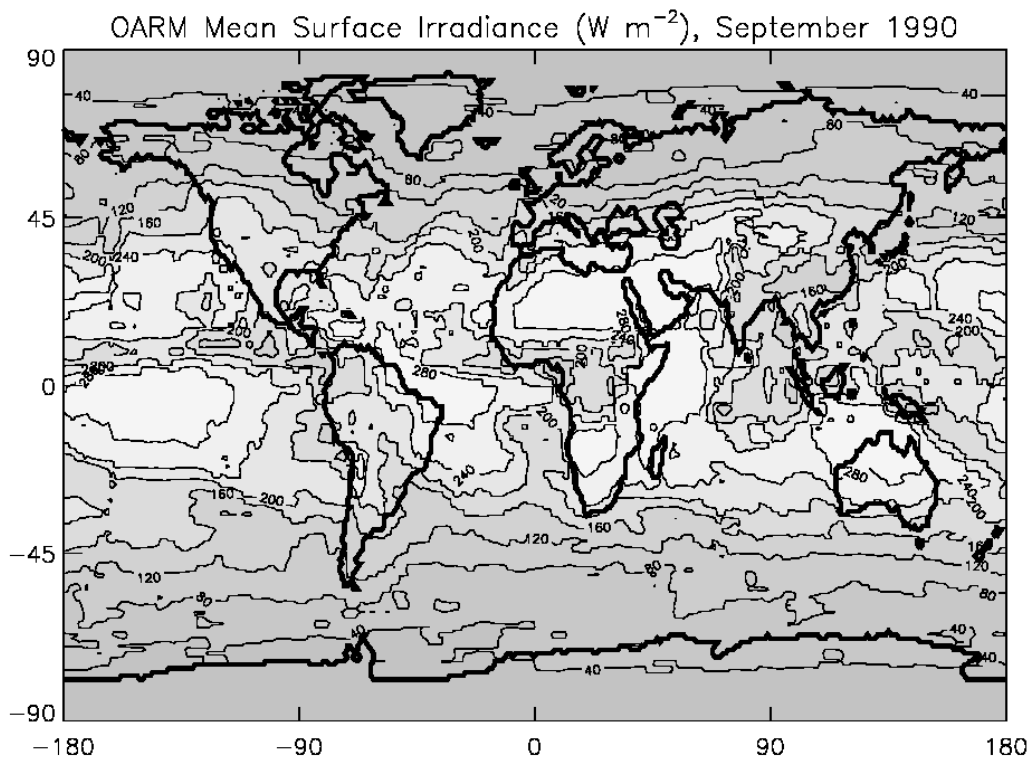
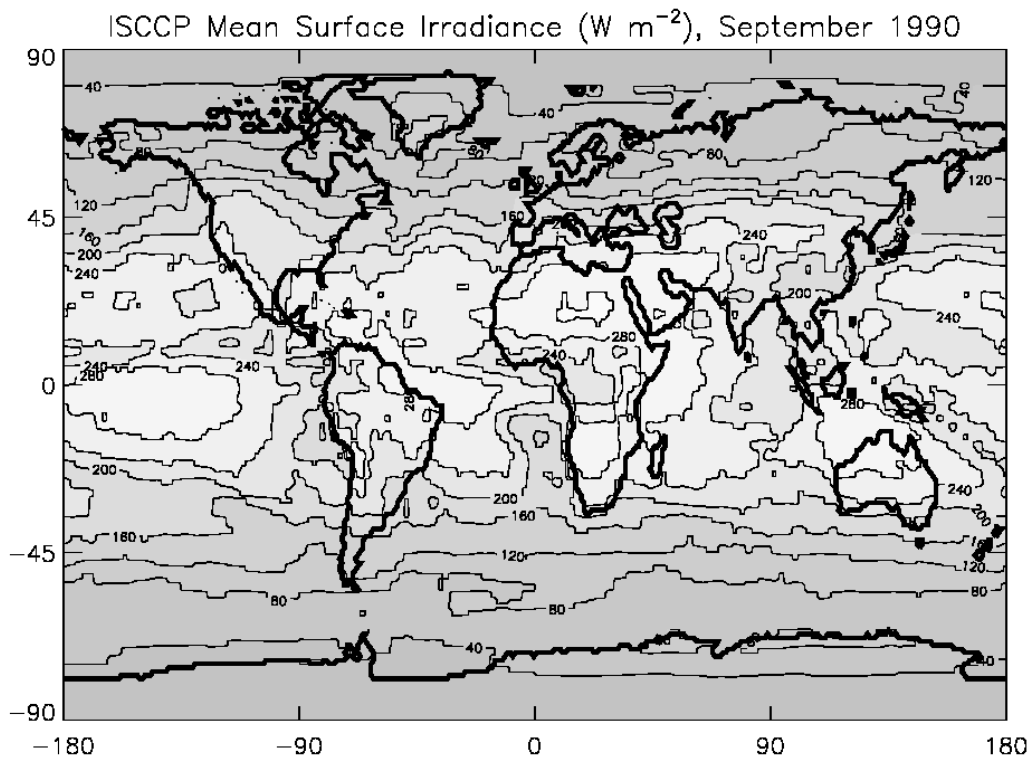


Figure 7. As in Figure 6 for September 1990.

References

- Aas, E., 1987. Two-stream irradiance model for deep waters. *Appl. Opt.* 26: 2095-2101.
- Ackleson, S.G., W.M. Balch, and P.M. Holligan, 1994. Response of water-leaving radiance to particulate calcite and chlorophyll *a* concentrations: A model for Gulf of Maine coccolithophore blooms. *J. Geophys. Res.* 99: 7483-7499.
- Ahn, Y.-H., A. Bricaud, and A. Morel, 1992. Light backscattering efficiency and related properties of some phytoplankters. *Deep-Sea Res.* 39: 1835-1855.
- Austin, R.W., 1974. The remote sensing of spectral radiance from below the ocean surface. In: *Optical aspects of oceanography*, N.G. Jerlov and E. Steemann-Nielsen, eds. pp 317-344, Academic Press.
- Bird, R.E. and C. Riordan, 1986. Simple solar spectral model for direct and diffuse irradiance on horizontal and tilted planes at the Earth's surface for cloudless atmospheres. *J. Clim. Appl. Meteorol.* 25: 87-97.
- Bishop, J.K.B., W.B. Rossow, and E.G. Dutton, 1997. Surface solar irradiance from the International Satellite Cloud Climatology Project 1983-1991. *J. Geophys. Res.* 102: 6883-6910.
- Bricaud, A., A.-L. Bedhomme, and A. Morel, 1988. Optical properties of diverse phytoplanktonic species: experimental results and theoretical interpretation. *J. Plank. Res.* 10: 851-873.
- Bricaud, A. and A. Morel, 1986. Light attenuation and scattering by phytoplanktonic cells: a theoretical modeling. *Appl. Opt.* 25: 571-580.
- Bricaud, A., Morel, A., and L. Prieur, 1983. Optical efficiency factors of some phytoplankton. *Limnol. Oceanogr.* 28: 816-832.
- Carder, K.L., R.G. Steward, G.R. Harvey, and P.B. Ortner, 1989. Marine humic and fulvic acids: their effects on remote sensing of ocean chlorophyll. *Limnol. Oceanogr.* 34: 68-81.
- Circio, J.A. and C.C. Petty, 1951. The near infrared absorption spectrum of liquid water. *J. Opt. Soc. America.* 41: 302-308.
- Daley, R., 1991. *Atmospheric data analysis*, Cambridge Univ. Press, Cambridge. 457 pp.
- Frouin, R., D.W. Lingner, and C. Gautier, 1989. A simple analytical formula to compute clear sky total and photosynthetically available solar irradiance at the ocean surface. *J. Geophys. Res.* 94: 9731-9742.
- Frouin, R., M. Schwindling, and P.-Y. Deschamps, 1996. Spectral reflectance of sea foam in the visible and near-infrared; In situ measurements and remote sensing implications. *J. Geophys. Res.* 101: 14361-14371.
- Gregg, W.W. and M.E. Conkright, 2001. Global seasonal climatologies of ocean chlorophyll: Blending in situ and satellite data for the CZCS era. *J. Geophys. Res.* 106: 2499-2515.
- Gregg, W.W. and K.L. Carder, 1990. A simple spectral solar irradiance model for cloudless maritime atmospheres. *Limnol. Oceanogr.* 35: 1657-1675.
- Han, Q., W.B. Rossow, and A.A. Lacis, 1994. Near-global survey of effective droplet radii in liquid water clouds using ISCCP data. *J. Clim.* 7: 465-497.
- Kalnay, E., and 21 others, 1996. The NCEP/NCAR 40-year reanalysis project. *Bull. Am. Meteorol. Soc.* 77: 437-471.

- Kasten, F., 1966. A new table and approximate formula for relative optical air mass. *Geophys. Bioklimatol.* B14: 206-223.
- Kiehl, J.T., J.J. Hack, G.B. Bonan, B.A. Boville, D.L. Williamson, and P.J. Rasch, 1998. The National Center for Atmospheric Research Community climate model: CCM3. *J. Clim.* 11: 1131-1149.
- Kirk, J.T.O., 1981. Estimation of the scattering coefficient of natural waters using underwater irradiance measurements. *Aust. J. Mar. Freshwater Res.* 32: 533-539.
- Maul, G.A., 1985. Introduction to satellite oceanography. Martinus Nijhoff Publishers, Boston, MA, USA., 606 pp..
- Moore, K.R., K.J. Voss, and H.R. Gordon, 1998. Spectral reflectance of whitecaps: Instrumentation, calibration, and performance in coastal waters. *J. Atmos. Oceanic Tech.* 15: 496-509.
- Morel, A., 1988. Optical modeling of the upper ocean in relation to its biogenous matter content (Case I waters). *J. Geophys. Res.* 93: 10749-10768.
- Morel, A. 1987. Chlorophyll-specific scattering coefficient of phytoplankton. A simplified theoretical approach. *Deep-Sea Res.* 34: 1093-1105.
- Morel, A. and A. Bricaud, 1981. Theoretical results concerning light absorption in a discrete medium, and application to specific absorption of phytoplankton. *Deep-Sea Res.* 28: 1375-1393.
- Norris, J.R., 2000. What can cloud observations tell us about climate variability? *Space Sci. Rev.* 94: 375-380.
- Pope, R.M. and E.S. Fry, 1997. Absorption spectrum (380-700 nm) of pure water. II. Integrating cavity measurements. *Appl. Opt.* 46: 8710-8723.
- Reynolds, R.W., 1988. A real-time global sea surface temperature analysis. *J. Clim.* 1: 75-86.
- Reynolds, R.W., C.K. Folland, and D.E. Parker, 1989. Biases in satellite-derived sea-surface temperatures. *Nature* 341: 728-731.
- Rossow, W.B., A.W. Walker, D.E. Beusichel, and M.D. Roiter, 1996. International Satellite Cloud Climatology Project (ISCCP): Documentation of new cloud datasets. 155 pp. Available on internet at <http://isccp.giss.nasa.gov/documents.html>.
- Sathyendranath, S. and T. Platt, 1988. The spectral irradiance field at the surface and in the interior of the ocean: a model for applications in oceanography and remote sensing. *J. Geophys. Res.* 93: 9270-9280.
- Sathyendranath, S., L. Lazzara, and L. Prieur, 1987. Variations in the spectral values of specific absorption of phytoplankton. *Limnol. Oceanogr.* 32: 403-415.
- Siegel, D.A., T.K. Westberry, and J.C. Ohlmann, 1999. Cloud color and ocean radiant heating. *J. Clim.* 12: 1101-1116.
- Slingo, A., 1989. A GCM parameterization for the shortwave radiative properties of water Cloud. *J. Atmos. Sci.* 46: 1419-1427.
- Smith, R.C. and K.S. Baker, 1981. Optical properties of the clearest natural waters (200-800nm). *Appl. Opt.* 20: 177-184.

Appendix. Mathematical description of the oceanic component of OARM.

The oceanic portion of OARM tracks three irradiance streams in the water column: downwelling direct, downwelling diffuse, and upwelling diffuse. We track only one scattering event for each of the oceanic layers for computational convenience.

The direct downwelling stream is modeled as

$$E_d(\lambda, k) = E_d(\lambda, k-1)T_{ad}(\lambda, k)T_{sd}(\lambda, k) \quad (A1)$$

where E_d is the downwelling direct spectral irradiance at level k in the water column (corresponding to the layer definitions of an OGCM, where $k = 1$ is the surface layer, and k is positive downward), T_{ad} is the spectral transmittance of the direct stream after absorption, and T_{sd} is the transmittance after scattering

$$T_{ad} = \exp(-a/\mu_d(\theta_w) \Delta z) \quad (A2)$$

$$T_{sd} = \exp(-b/\mu_d(\theta_w) \Delta z) \quad (A3)$$

(λ -dependences have been dropped), where a is the total absorption coefficient of the water in OGCM layer k , b is the total scattering coefficient, $u_d(\theta_w)$ is the average cosine, or path length in the water column as a function of the downwelling zenith angle θ_w , and Δz is the thickness of the OGCM layer in question. The downwelling zenith angle is related to the solar zenith angle θ by the index of refraction of seawater

$$u_d(\theta_w) = \cos\theta_w \quad (A4)$$

$$\theta_w = \sin^{-1}[\sin\theta/n]$$

where n is the seawater refractive index, parameterized as 1.341 (Austin, 1974).

The downwelling diffuse irradiance gains forward scattered downwelling direct irradiance and backscattered upwelling diffuse irradiance in the water column

$$E_s(k) = E_s(k-1)T_{as}(k)T_{ss}(k) + F[1 - T_{ss}(k)] + E_d(k-1)T_{ad}(k)\{F[1 - T_{sd}(k)]\} + E_u(k+1)T_{au}(k)\{B[1 - T_{su}(k)]\} \quad (A5)$$

where E_s is the downwelling diffuse irradiance at OGCM layer k , T_{as} and T_{ss} are the diffuse transmittances after absorption and scattering, respectively, F and B are the probabilities of forward and back scattering, respectively, T_{au} and T_{su} are the upwelling diffuse transmittances after absorption and scattering, respectively, and E_u is the upwelling diffuse irradiance. T_{as} , T_{ss} , T_{au} , and T_{su} are defined similarly to their downwelling direct counterparts, except that μ_d is replaced by μ_s for downwelling direct irradiance, and by μ_u for upwelling diffuse irradiance. They are considered constant in OARM at 0.83 (Sathyendranath and Platt, 1988) and 0.4 (Kirk, 1981), respectively. The first term on the right-hand side of Eq. A5 represents transmittance after scattering and absorption for the downwelling diffuse stream, plus the addition of the forward-scattered component. The second term represents forward scattering from the downwelling direct stream from the layer above, and the third term represents backscattered irradiance from the upwelling diffuse stream from the layer below. The backscattering probability B is defined as

$$B = b_b/b \quad (A6)$$

where b_b is the backscattering coefficient. The forward scattering probability is simply

$$F = 1 - B \quad (A7)$$

The diffuse upwelling stream is derived from the two-stream model of Aas (1987), with contributions from both the downwelling direct and downwelling diffuse explicitly

included, similarly to Ackleson et al. (1994). After experimentation, we found that the average cosine for downwelling diffuse irradiance μ_s could be substituted for the direct average cosine without incurring $> 1 \mu\text{M}$ quanta $\text{m}^{-2} \text{s}^{-1}$ error, except in the computation of irradiance leaving the ocean surface. With these assumptions, the integral form of the Aas (1987) model reduces to

$$E_u(k) = [E_d(k-1) + E_s(k-1)] \exp(\alpha \Delta z) (\alpha + c_s) / b_u \quad (\text{A8})$$

$$\alpha = 0.5 \{ (c_u - c_s) - [(c_s - c_u)^2 - 4(b_s b_u - c_s c_u)]^{1/2} \} \quad (\text{A9})$$

$$c_s = (a + r_s b_b) / \mu_s \quad (\text{A10})$$

$$c_u = (a + r_u b_b) / \mu_u \quad (\text{A11})$$

$$b_s = r_s b_b / \mu_s \quad (\text{A12})$$

$$b_u = r_u b_b / \mu_u \quad (\text{A13})$$

where r_s and r_u are dimensionless shape factors to represent the mean backscatter coefficient (Aas, 1987), and are assumed constant at 1.5 and 3.0, respectively (Ackleson et al., 1994).

Phytoplankton specific absorption coefficients $a^*_p(\lambda)$ are derived by taking spectra from the published literature and normalizing to the absorption at 440 nm [$a^*_p(440)$] to obtain normalized specific absorption spectra [$a^*_p(\lambda)$]_N for each of the five phytoplankton groups. Diatom and chlorophyte [$a^*_p(\lambda)$]_N are taken from Sathyendranath et al. (1987), cyanobacteria from Bricaud et al. (1988), coccolithophores from Morel and Bricaud (1981), and dinoflagellates from Ahn et al. (1992). Then the specific spectral $a^*_p(\lambda)$ values are derived using mean values at 440 nm. Diatom $a^*_p(440)$ represents the mean of 5 observations containing 4 different spp., chlorophytes 6 observations from 4 spp., cyanobacteria 5 observations from 3 spp., coccolithophores 3 observations of 1 spp., and dinoflagellates 1 spp, all from the references listed above. CDOM absorption is taken from Carder et al. (1989)

$$a_{\text{CDOM}}(\lambda) = C_h a^*_h(\lambda) + C_f a^*_f(\lambda) \quad (\text{A14})$$

where a_{CDOM} is the absorption coefficient of CDOM (m^{-1}), C represents the concentration (mg m^{-3}) of a humic acid component (subscript h) and a fulvic acid component (subscript f), and a^* is the specific absorption coefficient of the two components

$$a^*_h(\lambda) = 1.302 \times 10^{-4} \exp[450 - (\lambda)] \quad (\text{A15})$$

and

$$a^*_f(\lambda) = 5.0 \times 10^{-6} \exp[450 - (\lambda)] \quad (\text{A16})$$

(Carder et al., 1989). C_h and C_f are fixed as 1.0 and 10.0 mg m^{-3} , respectively (Ackleson et al., 1994).

Phytoplankton specific scattering coefficients are obtained from measurements at 590 nm and extended to the entire spectrum from information on specific attenuation coefficients (Bricaud et al., 1988). Diatom and chlorophyte specific scattering coefficient at 590 nm, $b^*_d(590)$ and $b^*_c(590)$, are the mean of 5 observations and 6 observations, respectively, from Morel (1987), Bricaud and Morel (1986) and Bricaud et al. (1988). Cyanobacteria $b^*_y(590)$ is the mean of 8 observations from Morel (1987), Bricaud and Morel (1986), Bricaud et al. (1988) and Ahn et al. (1992). Coccolithophore $b^*_o(590)$ is derived from the mean of 3 observations from Bricaud and Morel (1986), Bricaud et al. (1988), and Ahn et al. (1992). Dinoflagellate $b^*_f(590)$ is derived from a single observation by Ahn et al., (1992).

Measured chlorophyll-specific attenuation coefficients (Bricaud et al., 1988) suggested 1) a slight negative linear spectral trend for diatoms, 2) a spectrally flat profile for chlorophytes and coccolithophores, 3) a slight negative trend for cyanobacteria, with a local maximum corresponding to phycoerythrin absorption. But Bricaud et al. (1983) observed a strong spectral dependence for *Emiliana huxleyi*, which we adopt here. Given this information and knowledge of $c^*_p(590)$ for each phytoplankton group

$$c^*_p(590) = a^*_p(590) + b^*_p(590) \quad (\text{A17})$$

we fit the total attenuation spectra of Bricaud et al. (1988) by

$$c^*_d(\lambda) = c^*_d(590) - 4.3 \times 10^{-4}(\lambda - 590) \quad (\text{A18})$$

$$c^*_c(\lambda) = c^*_c(590) \quad (\text{A19})$$

$$c^*_y(\lambda) = c^*_y(590) - 8.0 \times 10^{-4}(\lambda - 590) \quad (\text{A20})$$

$$c^*_o(\lambda) = c^*_o(590) - 8.95 \times 10^{-4}(\lambda - 590) \quad (\text{A21})$$

$$c^*_f(\lambda) = c^*_f(590) \quad (\text{A22})$$

assuming no spectral dependence for dinoflagellates.

The specific total backscattering coefficients are derived by subtraction

$$b^*_i(\lambda) = c^*_i(\lambda) - a^*_i(\lambda) \quad (\text{A23})$$

where the subscript i indicates the phytoplankton group of interest, diatoms (d), chlorophytes (c), cyanobacteria (y), coccolithophores (o), and dinoflagellates (f).

Additionally, knowledge of the specific backscattering coefficient is required for the oceanic model. These values are derived from the probability of backscatter

$$b_b(\lambda) = B \times b(\lambda) \quad (\text{A24})$$

We assume no spectral dependence in b_b , and use a constant value of 0.002 for diatoms (Morel, 1988), 0.00071 for chlorophytes, 0.0032 for cyanobacteria (Ahn et al. 1992), 0.00071 for coccolithophores, and 0.0029 for dinoflagellates (both from Morel, 1988). Ahn et al. (1992) suggested a spectral dependence for cyanobacteria but generally none for the other groups.

Phytoplankton respond to the mean irradiance availability in the isopycnal layers in which they reside. This is especially important in an OGCM simulation with discrete numerical layers. OARM computes irradiance at the vertical boundaries of the model layers. Derivation of accurate mean irradiance within each model layer is essential for simulating realistic phytoplankton responses and primary production estimates in the context of variable cloud cover and thickness.

We approach this problem by deriving a lookup table of factors to convert irradiance at boundaries to the mean within the layer. The lookup table incorporates depth, chlorophyll concentration, and phytoplankton group as array indices. CDOM is assumed constant, but variability could be incorporated by addition of another dimension in the lookup table. The table is created applying the oceanic model in advance with the assumption that $\mu_d = 1$ uniformly. Computation of mean irradiance is

$$E_t \text{avg}(z) = M(\Delta z, \text{chl}, p) \{ [E_t(z-1) + E_t(z)] / 2 \} \quad (\text{A25})$$

where M is a factor obtained from the lookup table incorporating layer thickness (Δz), chlorophyll concentration (chl), and phytoplankton group (p), and E_t is the total irradiance. Note that this computation is non-spectral, although the computation of irradiance at the layer boundaries is spectral. The effect of the computation for average irradiance is not subtle – lookup table factors range from 0.0009 at high chlorophyll concentrations and 200 m layers to 0.95 at low chlorophyll and shallow layers (≤ 5 m).